

Microevents produced by gas migration and expulsion at the seabed: a study based on sea bottom recordings from the Sea of Marmara

J. B. Tary,^{1*} L. Géli,¹ C. Guennou,² P. Henry,³ N. Sultan,¹ N. Çağatay⁴ and V. Vidal⁵

¹*Ifremer, Marine Geosciences Department, 29280 Plouzané, France. E-mail: tary@ualberta.ca*

²*UMR 6538, Oceanic Domains, University of Western Brittany, European Institute for Marine Studies (IUEM), 29280 Plouzané, France*

³*CEREGE, Aix-Marseille University, CNRS, UMR 6635, 13545 Aix-en-Provence Cedex 4, France*

⁴*Mining Faculty, Geology Department, Istanbul Technical University (ITU), Maslak, 34469 Istanbul, Turkey*

⁵*Université de Lyon, Laboratoire de Physique, École Normale Supérieure de Lyon, CNRS, 69364 Lyon cedex 07, France*

Accepted 2012 May 2. Received 2012 April 29; in original form 2011 December 3

SUMMARY

Different types of 4-component ocean bottom seismometers (OBS) were deployed for variable durations ranging from 1 week to about 4 months in 2007, over soft sediments covering the seafloor of the Tekirdag Basin (western part of the Sea of Marmara, Turkey). Non-seismic microevents were recorded by the geophones, but generally not by the hydrophones, except when the hydrophone is located less than a few tens of centimetres above the seafloor. The microevents are characterized by short durations of less than 0.8 s, by frequencies ranging between 4 and 30 Hz, and by highly variable amplitudes. In addition, no correlation between OBSs was observed, except for two OBSs, located 10 m apart. Interestingly, a swarm of ~400 very similar microevents (based on principal component analysis) was recorded in less than one day by an OBS located in the close vicinity of an active, gas-prone fault cutting through the upper sedimentary layers. The presence of gas in superficial sediments, together with analogies with laboratory experiments, suggest that gas migration followed by the collapse of fluid-filled cavities or conduits could be the source of the observed microevents. This work shows that OBSs may provide valuable information to improve our understanding of natural degassing processes from the seafloor.

Key words: Time series analysis; Gas and hydrate systems; Body waves; Interface waves; Seismic attenuation; Wave propagation.

1 INTRODUCTION—GENERAL CONTEXT

The Sea of Marmara is located on the North Anatolian Fault zone in NW Turkey, a major transform-plate boundary that has produced devastating historical earthquakes along its 1600 km length. After the 1999 Izmit and Düzce earthquakes, the next large ($M_w > 7$) earthquake is expected close to the heavily populated (>15 million inhabitants) Istanbul Area (Fig. 1). Hence, the Sea of Marmara has been extensively surveyed during the last decade.

Several marine expeditions found gas emissions sites and brackish water seeps, along or near the main active faults scarps in the Sea of Marmara (Alpar 1999; Halbach *et al.* 2004; Armijo *et al.* 2005; Zitter *et al.* 2008; Géli *et al.* 2008). Moreover, recent sediment profiler (chirp) and multibeam echosounder data acquired during the MARMESONET cruise of *R/V Le Suroit* (Géli *et al.* 2010) show

the widespread presence of gas in the upper sediments and water column (Dupré *et al.* 2010; Tary 2011). Geochemical analysis indicates that the gas is mainly methane, and has two different origins: (1) in basins, gas is dominantly of bacterial origin, likely resulting from the decomposition of organic material in the Pleistocene sediments and (2) on the Western High and Central High (Fig. 1), gas is dominantly thermogenic, originating from the Eocene–Oligocene Thrace Basin source rocks (Bourry *et al.* 2009).

These observations and the high geohazard potential of the area are such that the Sea of Marmara has been identified as a unique, natural laboratory to study the relationships between fluids and seismicity through the EC-funded ESONET (European Seafloor Observatory Network) Network of Excellence. To prepare the implementation of permanent multidisciplinary seafloor observatories, two preparatory experiments were conducted in 2007 and 2009–2010. Here, we report observations of non-seismic microevents detected by ocean bottom seismometers (OBS) and show that these events are probably related to gas emissions from shallow sediment layers (<5 m). These findings may help to better understand degassing processes from the seafloor. In the perspective of future

*Now at: Department of Physics, University of Alberta, Edmonton, Alberta, T6G 2E1 Canada.

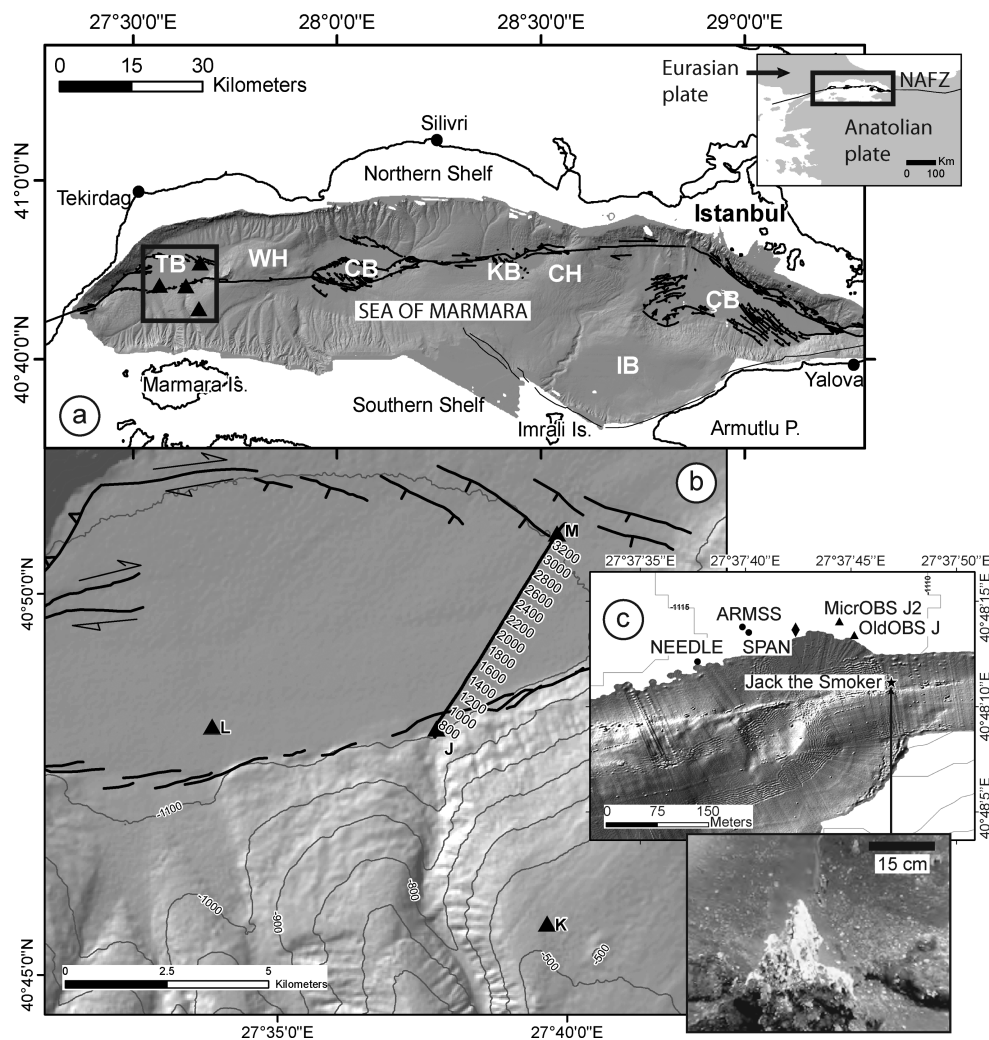


Figure 1. (a) Map of the Sea of Marmara with active fault traces (Imren *et al.* 2001; Rangin *et al.* 2001, 2004; Armijo *et al.* 2005). Abbreviations: NAFZ, North Anatolian Fault Zone; TB, Tekirdag Basin; WH, Western High; CB, Central Basin; KB, Kumburgaz Basin; CH, Central High; ÇB, Çınarcık Basin; IB: Imrali Basin; P, Peninsula; Is., Island. (b) Bathymetric map of the Tekirdag Basin. OldOBSs deployed during the MarNaut cruise in 2007 are indicated by black triangles. The black line with numbers corresponds to the ship track and trace numbers of the chirp profile in Fig. 5. The faults are indicated by the other black lines. (c) Zoom in the OBS network centre. Microbathymetric data were acquired during the MARMARASCARPS cruise in 2002 by the R.O.V. Victor (Armijo *et al.* 2005). OBSs provided by Ifremer and CGGVeritas are indicated by black triangles and black dots, respectively. The black star shows the location of ‘Jack the Smoker’ site where fresh water escapes from the seafloor through carbonate chimneys. The photograph taken by the R.O.V. Victor on the seafloor shows the outflow of fresh water as well as a fish on top of the main chimney. The white part of the chimney corresponds to bacterial mats. The black diamond shows the location of the seismic shot used for OBSs amplitude intercalibration (see Fig. S2).

multidisciplinary seafloor observatories, our results may also help establish a method to detect and characterize episodes of gas accumulation and release in shallow sediments.

2 INSTRUMENT CHARACTERISTICS AND ENVIRONMENTAL SETTINGS

Between 2007 May 14 and August 30, two different experiments were carried out in the western part of the Sea of Marmara with eight, autonomous OBSs of five different types: OldOBS, MicroOBS, ARMSS, SPAN, NEEDLE. The instrument locations, technical characteristics and recording periods are summarized in Table 1. Specific details, useful for the present paper, are given hereafter:

(1) OldOBS (deployed at sites J, K, L and M) are large instruments (1.5 m in height, weighing 240 kg) from Ifremer, de-

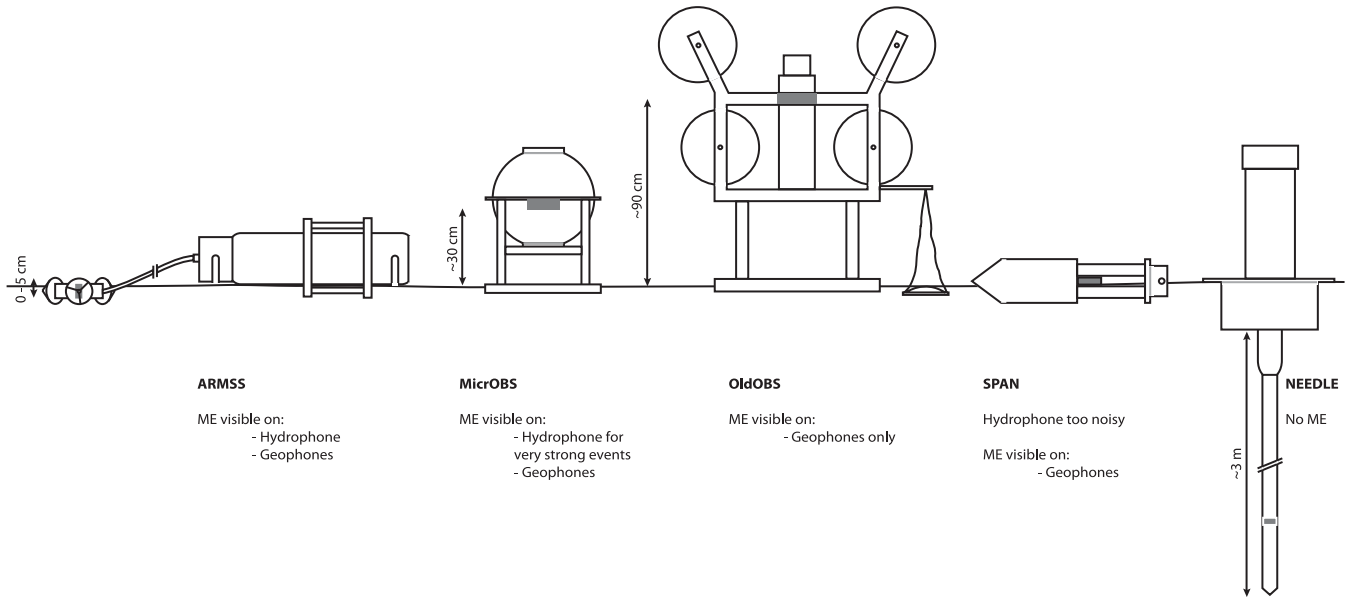
signed to be deployed offboard the operating vessel. The geophones (Geospace GS-11D, its response curve is given in Fig. S1 in the Supporting Information) are contained in an outer, pressure-resistant case resting on the seafloor, while the hydrophone is fixed on the instrument frame, ~ 0.9 m above the seafloor (Fig. 2).

(2) MicroOBS (deployed at site J2) is also an Ifremer instrument, weighing less than 20 kg, packaged within a 13” glass sphere, which includes the electronics, the batteries and the geophones (Geospace GS-11D). The hydrophone is fixed on the instrument frame, ~ 0.3 m above the seafloor. Like OldOBSs, MicroOBSs are deployed offboard the operating vessel.

(3) ARMSS (from CGGVeritas) consists of a 0.9 m long cylinder lying horizontally on the seafloor, with a head containing both the geophones (Geospace LT-101) and the hydrophone. The three geophones are arranged in a Galperin configuration, that is set orthogonally and all tilted at 54.7° to the vertical axis. A vibrating

Table 1. Position, technical characteristics, recording period, number of microevents recorded (N_{ME}) and N_{ME} per day for each OBS. F_0 , geophones natural frequency; F_s , sampling frequency; comp., component.

Stations	Long. (degree)	Lat. (degree)	Depth (m)	Recording period	F_0 (Hz)	F_s (Hz)	Observations	N_{ME}	N_{ME} day ⁻¹
J	E 27.62921	N 40.80372	1112	2007 May 14–August 30	4.5	250	–	915	8
J2	E 27.62902	N 40.80390	1112	2007 May 22–28	4.5	250	X comp. resonance	43	7
K	E 27.6608	N 40.7613	546	2007 May 14–August 19	4.5	250	–	3168	33
L	E 27.5645	N 40.8044	1132	2007 May 14–June 9	4.5	250	–	461	18
M	E 27.6637	N 40.8466	1110	2007 May 14–August 26	4.5	250	–	1534	15
ARMSS	E 27.62774	N 40.80382	1115	2007 May 14–June 9	14	500	–	1079	42
SPAN	E 27.62782	N 40.80376	1117	2007 May 14–28	4.5	500	Low quality	85	6
NEEDLE	E 27.62714	N 40.80337	1115	2007 May 14–28	4.5	500	–	0	0

**Figure 2.** Schematic structure of the OBSs deployed during the MarNaut cruise. For each OBS, the hydrophone location is indicated by the grey rectangle. ME, microevents.

system mounted around the instrument's head optimizes the coupling with the seafloor.

(4) SPAN (from CGGVeritas) is a ~ 1 m bullet shaped instrument, with geophones (SEND 'Full Tilt') integrated in a titanium container three-fourth buried in the soil, or a little more due to the soft character of sediments. The data of this instrument were too noisy to be used for quantitative signals analysis.

(5) NEEDLE (from CGGVeritas) consists of a 4.5 m long pipe inserted in the sediments. After penetration, a self-corroding system was activated, which divided the pipe into two mechanically decoupled sections, the sensors (three SEND 'Full Tilt' geophones and a hydrophone) being at the end of the lower section (~ 3 m long).

To test the different coupling devices, the five types of OBSs were all deployed for a maximum duration of 25 d, between 2007 May 14 and June 9. Although the Ifremer instruments (OldOBS and MicrOBS) were launched offboard *R/V L'Atalante*, the instruments provided by CGGVeritas (SPAN, ARMSS and NEEDLE) were installed *in situ* using *Nautile*, the submersible of Ifremer. The second experiment involved only the four OldOBSs of Ifremer, which were redeployed on 2007 June 9, to record the local microseismicity from the western Sea of Marmara (Tary *et al.* 2011).

Based on laboratory results obtained in comparable pressure and temperature conditions, linear corrections were applied to the instruments' internal clocks. For the first experiment, the drift of the internal clock was directly estimated for each instrument, based on GPS synchronization before deployment and after recovery, 25 d later. In addition, we took advantage of GPS-dated seismic shots recorded by the OBSs on 2007 May 23 and 24, which ascertained that the drift of the internal clocks were nearly linear during the first experiment. These shots were also used to improve the accuracy of the instruments' position. For the second experiment (2007 June 9–August 30), the direct estimation of the drift was not possible, because the OldOBS recordings stopped before the instruments' recovery. The drifts of the internal clocks during the second experiment were thus corrected by simply applying the clock drifts that were obtained for the first experiment.

Conversion factors, from digital (counts) into physical ($\mu\text{m s}^{-1}$ or Pa) units are unknown, except for the hydrophone of the MicrOBS and for the geophones of the OldOBSs. Hence, seismic shots have been used to calibrate the instruments' sensors relatively to the MicrOBS hydrophone and to the OldOBS geophones, which were used as references. Conversion factors were derived assuming that the peak-to-peak amplitude of the first *P*-wave train

in response to one given seismic shot, fired with the surface vessel directly above the OBSs (Fig. 1c), is the same for all OBSs (Fig. S2 and Table S1 in the Supporting Information). Necessary information for proper sensor calibration was only available for Ifremer instruments. Therefore, the instrumental response of the different sensors was not removed and the calibration is only an approximate one. The frequency response of Geospace GS-11D geophones (Fig. S1, OldOBS and MicrOBS) is almost flat in the frequency band of the microevents (4–30 Hz). The intercalibrated amplitudes given hereafter will be used to compare the different OBSs.

Three OldOBSs (K, L, M) were deployed so as to define a triangular network having equal sides, 10 km long, covering the North Anatolian Fault (Fig. 1). OBS L was placed on the bottom of the Tekirdag Basin, while OBS M was positioned in the northern part of the Tekirdag Basin, near WNW–ESE oriented normal faults (Le Pichon *et al.* 2001; Rangin *et al.* 2004) and OBS K was positioned on the southern side of the fault, in shallower water at a depth of 546 m. Based on sediment sounder profiler (chirp) data, gas prone sediment layers were documented immediately below OBSs K and M (Tary 2011).

The five remaining OBSs (OldOBS J, MicrOBS J2, ARMSS, NEEDLE and SPAN) were positioned near the foot of the southern flank of the Tekirdag Basin, at the centre of the network, within a distance of ~100–400 m from a cold seep called ‘Jack the Smoker’ sitting on the seafloor trace of the North Anatolian Fault (Armijo *et al.* 2005; Zitter *et al.* 2008). These OBSs are very close to each

other, the closest ones, ARMSS and SPAN, being separated by only 10 m (Fig. 1c).

3 MICROEVENTS GENERAL CHARACTERISTICS AND INTERPRETATION

The data set was first analysed to characterize the microseismicity in the area. The results were published in Tary *et al.* (2011). Over the whole period, 270 seismic events (recorded at least at 3 stations) were identified using a short-term average (STA)/long-term average (LTA) detection algorithm.

The OBSs also recorded a large number of microevents that were not detected by the above mentioned procedure, as they are generally not recorded by more than one station although their peak amplitude is comparable to the one of local microearthquakes (Fig. 3 and Fig. S3 in the Supporting Information).

Generally, microevents have: (1) short durations, ranging from 0.3 to 0.8 s in average, (2) frequency spectra between 4 and 30 Hz, (3) a large amplitude range of two orders of magnitude and (4) no clear secondary arrival. Microevents characteristics change slightly depending on the instrumental response of each OBS type (Fig. S3). Signals recorded by OldOBSs have higher frequency contents (5–30 Hz) and shorter durations (0.1–0.6 s) than that of the other instruments (4–12 Hz, 0.5–0.8 s).

Except NEEDLE, all instruments have recorded microevents (NEEDLE only recorded aseismic signals related to its

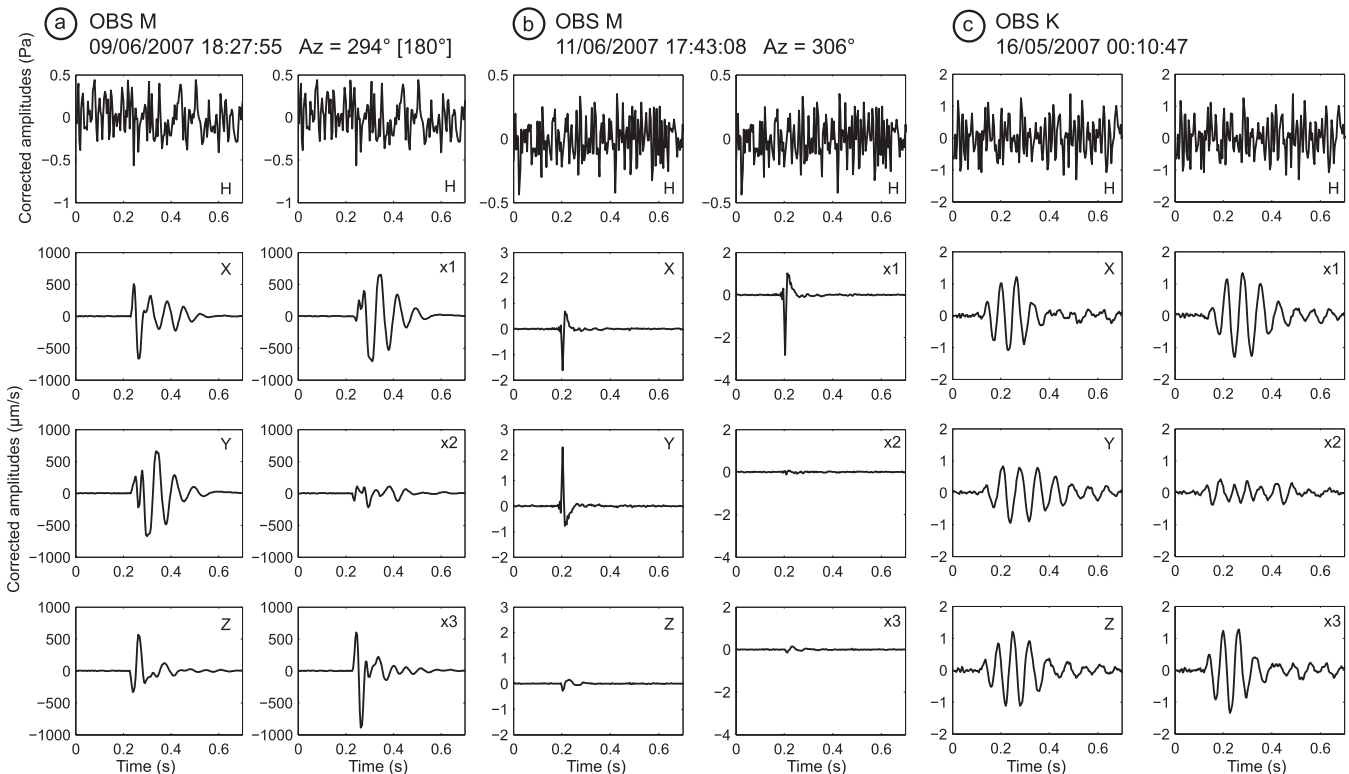


Figure 3. Three examples of microevents recorded by either OBS M or OBS K. The three-components seismograms are presented before (H, hydrophone; X and Y, horizontal components; Z, vertical component) and after rotation in the frame of reference of the polarization ellipsoid (components x1, x2 and x3). Azimuths were calculated using eq. (2) (see Section 4.2 for explanations). (a) Microevent recorded by OBS M on 2007 June 9 at 18:27:55 with corrected amplitudes of few hundreds of $\mu\text{m s}^{-1}$. (b) Microevent recorded by OBS M on 2007 June 11 at 17:43:08 with corrected amplitudes of a few $\mu\text{m s}^{-1}$. This microevent is typical of the ones constituting the swarm. Note that the two microevents have similar azimuth. (c) Microevent recorded by OBS K on 2007 May 16 at 00:10:47 with corrected amplitudes similar to the microevent presented in (b). Amplitudes were corrected according to the methodology described in Section 2. Note the difference in polarization between the microevents shown in (a) and (c) (plane x1–x3), and the microevent shown in (b) (component x1).

post-penetration stabilization mainly during the first two days of the experiment), discarding the hypothesis of instrumental noise to explain their origin. The absence of microevents in the NEEDLE records can be explained by the occurrence of gassy sediments directly in contact with the geophones. The additional impedance contrast at the surface of the buried pipe created by a thin film of fluid partially reflects the wave, and thus prevents this instrument to record the microevents.

The microevents are visible on the hydrophones only when these are close enough to the sediments surface. The hydrophones of ARMSS and J2, situated at the seafloor and ~ 30 cm above the seafloor, respectively, recorded only microevents having amplitude on the vertical geophone exceeding $\sim 2\text{--}3 \mu\text{m s}^{-1}$ (ARMSS) and $\sim 15 \mu\text{m s}^{-1}$ (J2). Earthquakes and seismic shots with lower amplitudes on the vertical geophone ($\sim 1 \mu\text{m s}^{-1}$) are clearly visible on all hydrophones. The absence or low amplitudes of the signals recorded by hydrophones appear to be specific to microevents. This could be explained by a propagation mainly along the water-sediment interface, transmitting very little motions to the water column. Hydrophones from other OBSs (OldOBS and NEEDLE) would be too far from the water-sediment interface to be able to record any microevents.

The microevents are most of the time not correlated from one OBS to another, implying that the source is in very close vicinity of the OBS. Some strong microevents are simultaneously recorded only by the closest stations, ARMSS and SPAN which are 10 m apart (Fig. S3). These pairs of signals present very different waveforms and frequency content likely due to the strong resonance of OBS SPAN geophones around their natural frequency (4.5 Hz, Fig. S3). No location was attempted because of the poor quality of OBS SPAN recordings that involves large time picks uncertainties. On the other hand, J2 and J, 25 m apart, did not record any correlated microevents. The maximum spacing between two OBSs to simultaneously record microevents of average amplitude is less than 10 m. Thus, microevents seem to be strongly attenuated both horizontally in the sediments and vertically in the water column.

The number and temporal distribution of microevents recorded by each instrument are shown in Table 1 and Fig. 4. About 7300 microevents were detected. The number of microevents is variable from one OBS to another. For instance, OBSs J and K, two OldOBSs with approximately the same recording period, recorded 915 and 3168 microevents, respectively (Fig. 4 and Table 1).

No clear cycles, as the tidal cycles [less than 10 cm in the Sea of Marmara (Alpar & Yüce 1997)], are visible on the microevents temporal distribution. In addition, no clear correlation between the number of microevents and the hour of the day has been found, as it could be expected if these signals resulted from the activity of some living organisms (Fig. S4, Supporting Information).

Comparable non-seismic microevents of short duration are very common on OBS recordings, but seismologists have paid little attention to these signals, as no useful correlation for seismological purposes can be made between distant instruments. Buskirk *et al.* (1981), Diaz *et al.* (2007) and Sohn *et al.* (1995) have reported very similar signals in varying environmental and geodynamical settings, that is the Pacific Rim borders, the Galicia passive margin and the Southern Juan de Fuca ridge, respectively. These studies reported signals with: durations between 0.5 and 1 s in the case of Diaz *et al.* (2007) and Sohn *et al.* (1995), and between 0.5 and 4 s in the case of Buskirk *et al.* (1981); frequency contents constituted by narrow peaks between 3 and 30 Hz; no clear secondary arrivals; and large differences in the number of microevents recorded by different OBSs. In addition, no correlation was found between microevents

recorded by two different OBSs. The signals reported by Buskirk *et al.* (1981) have longer durations in average, are monochromatic and show a progressive decrease of the coda amplitude. The latter could be due to the instruments' resonance, although Buskirk *et al.* (1981) also noted that the frequency content of the recorded signals is different for the same OBS deployed at different sites.

The above observations rule out the hypothesis that the microevents we observe could result from instrumental noise. Buskirk *et al.* (1981) claimed that the number of microevents depends on the hour of the day for instruments at depths shallower than 1000 m. In addition, the number of events decreases with the depth of the instrument, suggesting a possible relationship with the vertical distribution of biomass in the ocean. Last but not the least, no microevents were recorded within boreholes, or other environments unfavourable for fish activity. These observations, and the recovery of living organisms (eggs of unknown origin) attached to two OBSs, lead Buskirk *et al.* (1981) to suggest a biological origin of the signals.

Another argument supporting the hypothesis of biological activity could be that the number of microevents recorded by OldOBS K (water depth ~ 546 m) is two to three times greater than the number of microevents recorded by OldOBSs J, L and M (water depth ~ 1000 m). However, besides biologic activity, pressure effects on gas bubbles can also explain the decrease in the number of microevents with depth. Indeed, gas solubility decreases with pressure, resulting in an increase in bubble size and gas exsolution. Hence, for a same gas source and similar sediments, more bubbles will be created at lower pressure (i.e. at shallower depths). So, a decrease of biological activity is not the only parameter that could explain the decrease of the number of microevents with depth.

Non-biological explanations for the microevents are also far more likely for the following reasons. First, a total of 30 dives with Nautilie submersible were conducted in 2007 to explore the Marmara deep seafloor (Henry & MarNaut Cruise Sci. Party 2007), showing the relative scarcity of fish activity near the sea bottom. Secondly, the occurrence of microevents does not show any cyclicity, nor any clear dependence on the hour of the day (Fig. S4), while fish are supposed to have an internal biological clock (Bone & Moore 2008). Thirdly, swarm of microevents share relatively common characteristics (e.g. similar duration, frequency content, waveform), whatever the instrument design and during extended periods of time. As pointed out by Diaz *et al.* (2007), 'the observation of events with very different amplitudes but very similar waveforms and the existence of clearly differentiated clusters of events, seem to discard a biological origin'.

As mentioned earlier, the origin of the microevents is very close to the instruments. Therefore, regional phenomena, such as tectonics or distant sources (e.g. related to human activity) can be discarded. In addition, sources in the water column [deep currents, resonating clouds of bubbles (Pontoise & Hello 2002), *T* waves (Talandier & Okal 1996) and explosions/implosions] are very unlikely because microevents were not recorded by OldOBS hydrophones. A relationship between deep currents and microevents is also very unlikely because deep sea currents in the Sea of Marmara are, to some extent, a quasi-steady state phenomenon, and cannot explain the characteristics of the observed microevents.

On the other hand, gas is known to be common in marine sediments, and the Sea of Marmara is not an exception. Active venting sites have been found throughout the Sea of Marmara by geophysical means (Alpar 1999; Géli *et al.* 2008; Dupré *et al.* 2010) and visual observations (Zitter *et al.* 2008). A chirp profile, crossing the

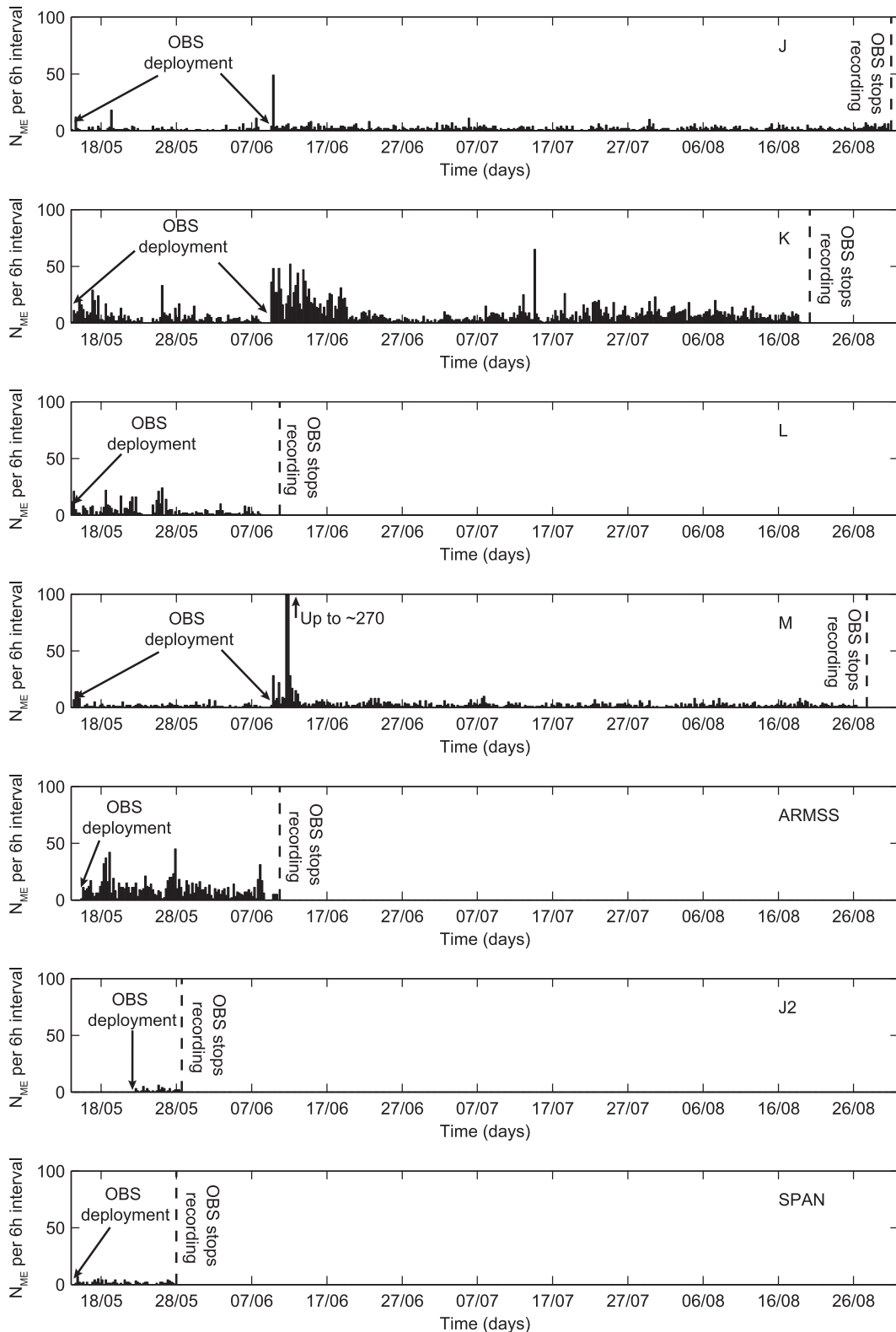


Figure 4. Temporal evolution of the number of microevents recorded by OBSs J, K, L, M, ARMSS, J2 and SPAN. N_{ME} , number of microevents.

position of OBS J and M, was collected during the MARMESONET cruise in 2009 (Géli *et al.* 2010, Fig. 5). On this profile, a high-amplitude reflector followed by a strong attenuation of the seismic waves is clearly visible close to the fault situated below OBS

M. These signatures are characteristic of the presence of gas. In addition, experiments and modelling (Chouet 1986, 1988, 1996; Ferrazzini *et al.* 1990; Vidal *et al.* 2006; Diaz *et al.* 2007; Varas *et al.* 2009) of the opening and resonance of a cavity filled by fluids

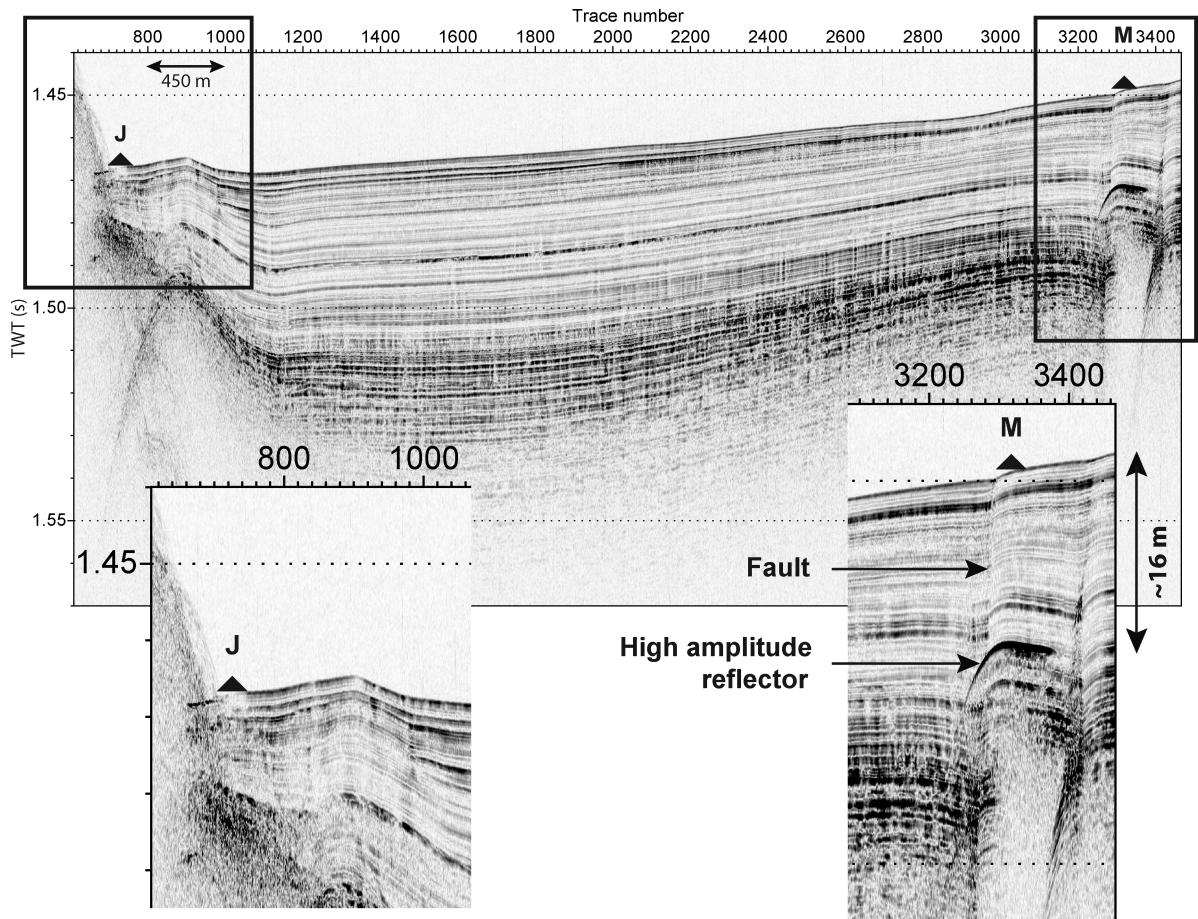


Figure 5. Chirp profile acquired during the MARMESONET cruise in 2009 November–December (Géli *et al.* 2010, see location in Fig. 1). OBSs J and M are indicated on the profile by black triangles. Below M is visible a high amplitude reflector followed by a strong attenuation of the seismic waves (zoom on the right). No seismic anomaly is visible below J (zoom on the left).

generate signals with waveforms qualitatively consistent with our data.

Hence, in the following we suggest that the microevents could result from gas migration in the seafloor, considering (i) the presence of gas and a fault near OBS M (where the swarm of microevents was recorded) and (ii) modelling of source and wave propagation. The source of the microevents is likely quite superficial, as no correlation is observed from one OBS to another, unless they are less than 15 m apart.

4 SPECIFIC CLUSTER SEQUENCE ON OBS M

4.1 Sequence chronology

Interestingly, OBS M recorded a swarm of 400 microevents in 24 h on June 11 and 12 (Fig. 6). Despite large amplitude differences, the microevents recorded during this crisis have very similar waveforms (Fig. S5, Supporting Information) and frequency contents (dominant frequency between 10 and 20 Hz). The number of microevents increases gradually over the crisis, reaching a maximum after 6 h with 96 microevents in 2 h (the background rate was ~ 5 microevents h^{-1}).

About two days before the swarm of microevents, a very strong microevent with a peak-to-peak amplitude $>1000 \mu\text{m s}^{-1}$ was

recorded by OBS M (Figs 3a and 6). Despite its very high amplitude, the signal is not visible on the hydrophone.

As it occurred only ~ 40 min after OBS M hits the sea bottom (2007 June 9; 17:48:04), it seems likely that the impact of the instrument on the seafloor has indirectly caused this strong signal. The impact may also have significantly destabilized the gas prone sediments close to the OBS, causing gas expulsion from the superficial sediments. A similar process could also explain the increase in the number of microevents just after the redeployment of OBSs J, K and M.

Then, after about 40.5 h of relative quiescence, OBS M recorded the swarm. This phase constituted by signals of relatively low amplitudes could correspond to gas-related processes within the superficial sediments.

4.2 Wave polarization analysis

First, the signals were detected with an automatic algorithm based on a STA/LTA threshold and visually controlled. Secondly, for each microevent, one temporal series of N samples was extracted to control the origin time and average. The three-component temporal series in the OBS frame of reference were rotated in the wave frame of reference using a method based on Jurkevics (1988) for wave polarization analysis. The covariance matrix was calculated over

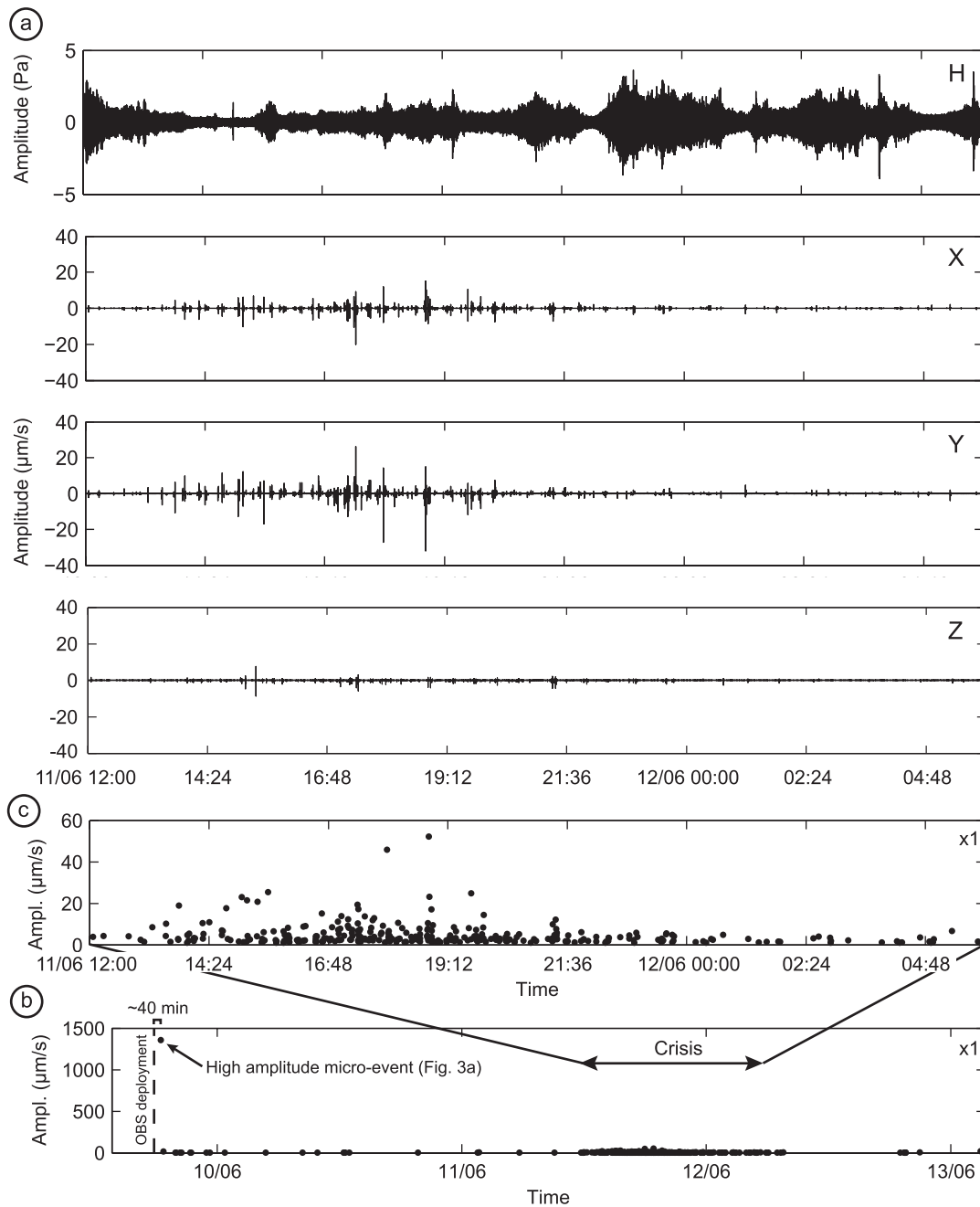


Figure 6. (a) Recordings of OBS M during the crisis of microevents, June 11 12:00–12 06:00 (H: Hydrophone; X and Y: horizontal geophones; Z: vertical geophone). Peak-to-peak amplitudes of the microevents recorded on OBS M for the x1 component: (b) three-day sequence after deployment (2007 June 10–13), (c) during the crisis.

the complete signal by

$$[S_{nm}] = \sum_{t=1}^N f_n(t) f_m(t), \quad (1)$$

with N is the number of samples, f is the temporal series and f_n and f_m are the signal components on x , y or z .

Then, the eigenvectors (\mathbf{u}_1 , \mathbf{u}_2 and \mathbf{u}_3) together with their corresponding eigenvalues (λ_1 , λ_2 and λ_3) were determined from this symmetric 3×3 covariance matrix. The three pairs eigenvector–eigenvalue correspond to the polarization ellipsoid that best fit the data. As the type of waves corresponding to microevents

is not known *a priori*, the temporal series were only multiplied by the three eigenvectors to rotate the signals in the frame of reference of the polarization ellipsoid (components x1, x2 and x3) (Fig. 3).

In this frame of reference, the polarization of the microevents presented in Fig. 3 is very different. In one case, the particle motion is mainly in the x1–x3 plane (Figs 3a and c), which is consistent with surface waves [Stoneley–Scholte waves, e.g. Favretto-Anrès & Rabau (1997), Zakharia (2002)]. In the other case, the particle motion is linear in the x1 direction (Fig. 3b), which in principle is consistent with both P and S waves. In addition, considering the frequency content of microevents, the P - and S -waves velocities in superficial sediments (see Section 5), and a realistic source–receiver

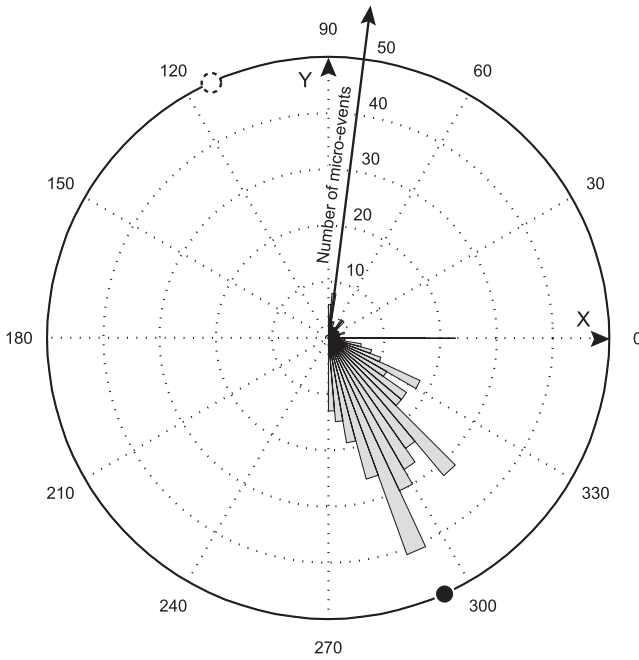


Figure 7. Azimuths of the first eigenvector of the polarization ellipsoid in the OBS frame of reference determined for the microevents constituting the crisis recorded on OBS M. OBS horizontal components X and Y are directed towards 0° and 90° , respectively. Numbers near the dotted circles inside the diagram indicate the number of microevents. Each grey bin represents 5° . The azimuth of the high amplitude microevent presented in Fig. 3(a) [294° (180°)] is indicated by the black dot. This event being possibly a S wave significantly affected by near-field waves or an interface wave, the 180° ambiguity in azimuths calculation was not resolved (white-dashed dot).

distance of less than 15 m, near-field effects should dominate microevents waveforms. These effects will ultimately make P and S waves arrivals undistinguishable (e.g. Lokmer & Bean 2010). Near-field effects also affect the polarization of body waves. Close to the source, both P and S waves can present ‘quasi-elliptical’ polarization due to the superposition of near-field waves to the far-field wave trains (Vavryčuk 1992). Thus, microevents showing a non-linear polarization are not necessarily surface waves, but could also correspond to body waves significantly disturbed by the presence of near-field waves. This could explain the absence of the very high amplitude microevent on hydrophone recordings if this signal is mainly composed by an S wave (Fig. 3a). The source radiation pattern, which in principle could indicate which types of waves are expected depending on the source and receiver locations, was not used here due to the lack of information about the geometry of the source of microevents.

Azimuths of the principal eigenvector \mathbf{u}_1 of the polarization ellipsoid for all micro-events of the swarm were obtained using

$$Az = \tan^{-1} \left(\frac{\mathbf{u}_1(y) \text{ sign}(\mathbf{u}_1(z))}{\mathbf{u}_1(x) \text{ sign}(\mathbf{u}_1(z))} \right). \quad (2)$$

The sign of the vertical component of the principal eigenvector is included in eq. 2 to resolve the 180° ambiguity in azimuths calculation. The azimuth of the signal presented in Fig. 3(a), polarized in the x_1 – x_3 plane, was determined by eq. (2) using only the horizontal components of \mathbf{u}_1 . The 180° ambiguity in azimuths calculation was not resolved in this case. These azimuths in the OBS frame of reference are shown in Fig. 7. The orientation of the principal eigenvector is very stable over the crisis, around 285° – 315° in the

OBS frame of reference, suggesting a localized source. Azimuths calculated for the other two eigenvectors show no preferential orientation, as expected if very little wave energy is focused on these components.

Notably, the strong microevent and the microevents constituting the swarm recorded by OBS M have similar azimuths, 294° [180°] and 285° – 315° , respectively. One possibility is that both could be related to fluid migration along the fault that is visible on the chirp profile located close to OBS M (Fig. 5).

4.3 Principal component analysis (PCA)

To find the common features of microevents and propose some physical explanations, a PCA was applied to determine the most characteristic microevents of the swarm. Before the calculation of the PCA, the signals were rotated in the frame of reference of the polarization ellipsoid following the method described in Section 4.2. The covariance matrix between all signals, with a common origin and a zero-average, was calculated following this formula,

$$[C_{tp,tq}] = \sum_{1 \leq i, j \leq M} f_i(t_p) f_j(t_q), \quad \text{where } t_1 \leq t_p, t_q \leq t_N, \quad (3)$$

with f_i and f_j are the temporal series, M is the number of microevents and N is the number of samples.

Eventually, the characteristic signals (eigenvectors, \mathbf{V}_i , $i = 1, M$) and their data representativeness (eigenvalues, λ_i , $i = 1, M$) are calculated from the covariance matrix. Hereafter, the representativeness of each eigenvector will be given as a percentage of the total energy ($\lambda_i^2 / \sum \lambda_i^2$).

The microevents constituting the swarm recorded by OBS M on June 11 and 12 present four particularities: (i) they are very impulsive; (ii) of short duration (mainly around 0.1 s); (iii) very similar and (iv) present higher amplitudes on the horizontal components than on the vertical one (Fig. 3b). The PCA performed with this data set indicates that the first eigenvector has a data representativeness of ~ 83 per cent on the x_1 component (Fig. 8), suggesting a common source and similar source-receiver ray paths. The relatively low data representativeness of the first eigenvectors of the x_2 and x_3 components, ~ 35 and 58 per cent, respectively, result likely from the presence of coherent arrivals of smaller amplitudes, such as near-field waves, modifying the otherwise linear polarization of these microevents.

The characteristic signal is very impulsive and has a duration of around 0.15 s on the x_1 component. Frequency spectra of the eigenvectors of the three components show one main peak between 13 and 20 Hz. Notably, the frequency spectrum of the first eigenvector of the x_1 component show a higher frequency content than the other components (Fig. 8). The main characteristics of the first eigenvectors are summarized in Table 2.

The PCA was also applied to the complete data set. Most of the first eigenvectors have a frequency spectrum with one dominant frequency, between 5 and 23 Hz for Ifremer OBSs (J, K, L, M and J2) and around 10 Hz for OBS ARMSS (Table S2 and Fig. S6 in the Supporting Information). Considering only the x_1 component, more than 80 per cent of the microevents energy corresponds to the first five eigenvectors (i.e. five families). The microevents could then be grouped in families as in Diaz *et al.* (2007), the characteristics of these families being slightly different from one OBS to another (Fig. S6).

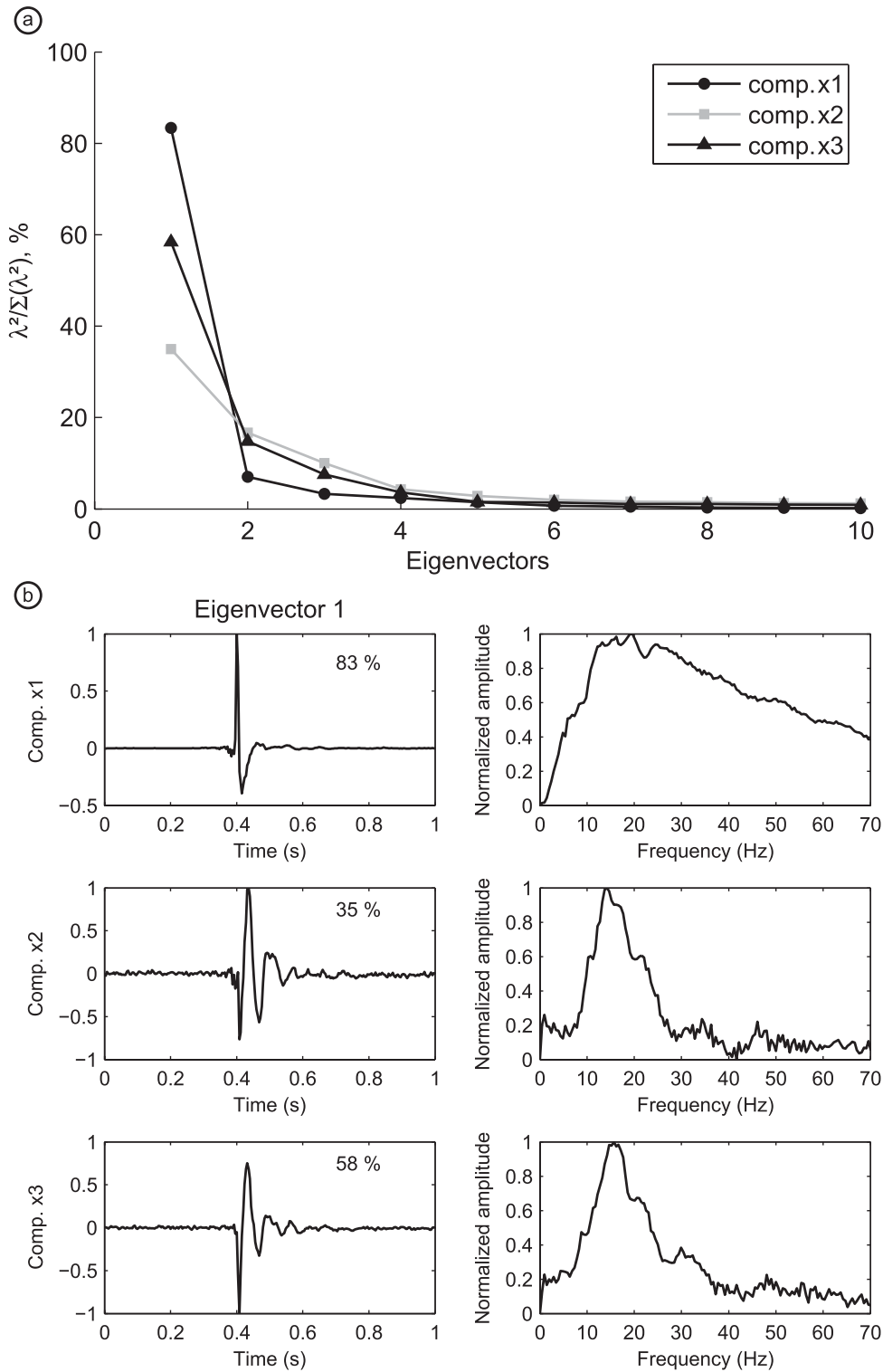


Figure 8. PCA of the microevents constituting the crisis identified on OBS M for the components x1, x2 and x3. (a) Representativeness of the first 10 eigenvectors. (b) Temporal series of the first eigenvectors. The representativeness of each eigenvector is indicated by its eigenvalue given in percentage of the total energy. The eigenvector spectrum is given on the right.

5 SOURCE AND WAVE PROPAGATION MODELLING

The numerical simulations were carried out using the SKB code (Dietrich 1988). This code computes, as a function of frequency

and wave number, the response in terms of stress and displacement of a 3-D, horizontally stratified, half-space subjected to a source positioned anywhere in the stratification. Fluid layers within or bounding the stratification can be taken into account. The attenuation is included by working with complex wave velocities (Toksöz & Johnston 1981). The computation is based on a recursive algorithm

Table 2. First eigenvector characteristics of the PCA performed on the microevents of the swarm recorded by OBS M. The number of microevents used in the PCA is also indicated (ME, microevents). Per cent, data representativeness (energy); Freq., dominant frequency; Dur., duration.

Eigenvector 1			
Components	Per cent	Freq. (Hz)	Dur. (s)
OBS M swarm (368 ME)			
x1	83	13–20	0.14
x2	35	14.2	0.21
x3	58	14.5–17	0.23

using reflection–transmission coefficients as wave vector propagators (Kennet & Kerry 1979). The last steps of the computation are to integrate in discrete wave numbers (Bouchon 1981), and to make a convolution with a spectrum of a signal source followed by an inverse Fourier transform in time, to recover stresses and displacements in space and time.

According to Biot (1956), water saturation induces an attenuation that can be accounted for by a complex formulation of wave velocities, as in viscoelastic media [see also Géli *et al.* (1987)]. Therefore, our computation method is adapted to the modelling of wave propagation in strongly attenuating, marine subsurface sediments, (e.g. Meunier & Guennou 1991). This computation method takes into account the complete wavefield (direct, transmitted and reflected waves), including both far- and near-field terms (Dietrich & Bouchon 1985). The representation of the source in terms of forces or moment tensor appears within the SKB code in terms of equivalent stress or displacement discontinuity, allowing the calculation of stress and displacement at the receivers by using reflection–transmission coefficients. The source signal used is the zero-phase Ricker signal.

The model consists of a 1110 m thick water layer, with typical density of 1000 kg m^{-3} and P -wave velocity of 1500 m s^{-1} , overlying a homogeneous half-space. Sediments P -wave velocity and density measured on cores (using a Geotek Multi-Sensor Core Logger—MSCL; Geotek, Daventry, UK) collected near OBS J have been used for the numerical seismograms calculation (Fig. S7, Supporting Information). The acoustical properties of the homogeneous half-space correspond to those of a soft and very attenuating sediment, that is a density of 1500 kg m^{-3} , P -wave velocity and quality factor of 1550 m s^{-1} and 10, S -wave velocity and quality factor of 100 m s^{-1} (Sultan *et al.* 2007) and 10 (Wang *et al.* 1994; Campbell 2009). Three types of point source were tested: an isotropic explosive source generating P waves with the same energy in all directions, and two unidirectional forces generating P waves with the maximum of energy in the horizontal and vertical directions. A two-component source (isotropic and single force) in an elastic half-space was studied by Kanamori *et al.* (1984) for the case of the rupture of a ‘lid’ on top of a cylinder. In the near-field, they show that the isotropic part of the source can be neglected when the radius of the cylinder is small compared to the source–receiver distance. In our case, the conduits radius, inferred from the bubble size at the seafloor, is less than 1 cm, while the source–receiver distance ranges between 1 and 10 m, resulting in a ratio of ~ 0.001 – 0.01 . Hereafter, the waveform modelling using an isotropic source is given for comparison.

In all simulations, the source signal has a constant frequency content of 15 Hz, consistent with the observed microevent frequency content. Numerical seismograms were calculated for 100 horizontally aligned receivers (spaced by 1 m) at four different depths

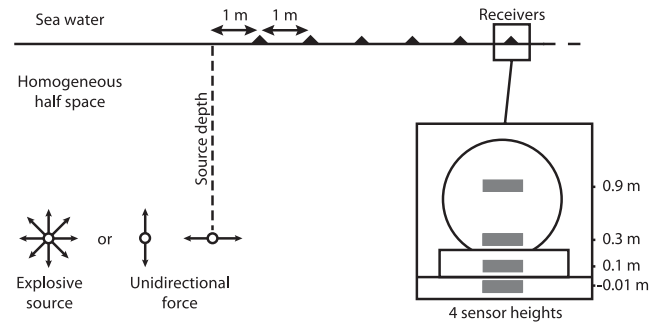


Figure 9. Configuration of the model used for microevent modelling. A point source (unidirectional force or explosive) located in a homogeneous half space produces either P or interface waves recorded by a set of equally spaced receivers on the surface (four sensor heights: 0.01 below and 0.1, 0.3 and 0.9 m above the interface).

(0.01 m below and 0.1, 0.3, 0.9 m above the water–sediment interface), and two source depths, 2 and 5 m below the water–sediment interface (Fig. 9).

Whatever the type and depth of the source, the computed signals are attenuated very quickly in the sediments (Fig. 10). Surface waves (Stoneley–Scholte waves) are produced by both unidirectional forces and the explosive source in superficial sediments. These waves, propagating at $\sim 77 \text{ m s}^{-1}$ in our configuration, are attenuated both horizontally in sediments and vertically in the water column (Figs 10 and 11). However, in the case of an explosive source, P waves with significant amplitudes are clearly visible on the horizontal component.

The microevent shown in Fig. 3(c) has about the same amplitude on the x1 component than on the x3 component, which could be compatible with Stoneley–Scholte waves produced by a shallow source.

The impulsive microevents of the crisis have most of their energy on the x1 component and thus cannot be interpreted as Stoneley–Scholte waves (Fig. 3b). They could in principle be better explained by a P or an S wave hitting the sediments–water interface with a high incidence angle, transmitting little energy to the water column. The corresponding wavelength would be of the order of 100 m and 6.7 m, respectively, which is probably much more than, or in the order of, the distance to the source. Most likely, these impulsive signals are generated by a weak but very close source causing horizontal displacement, which could be a pulsing conduit.

6 PHYSICAL HYPOTHESES AND INTERPRETATION

6.1 Physical hypotheses

Bubbles in sands are spherical, grow and migrate by displacing grains, whereas bubbles in clay are presumably oblate spheroid, and migrate by fracturing the sediments (Johnson *et al.* 2002; Boudreau *et al.* 2005). Hence, gas migration in fine-grained sediments is expected to depend on fracture propagation, which is a function of the mechanical properties of the medium through its Young’s modulus E , shear strength and fracture toughness K_{1c} (van Kessel & van Kesteren 2002; Algar & Boudreau 2009). However, it is often observed at the seafloor that bubbles escape continuously through tubular conduits, which are sometime recovered by cemented chimneys in the sediments. Such open conduits may be maintained to a few meters depth in the sediment and enable bubble-induced pore water mixing (Haeckel *et al.* 2007).

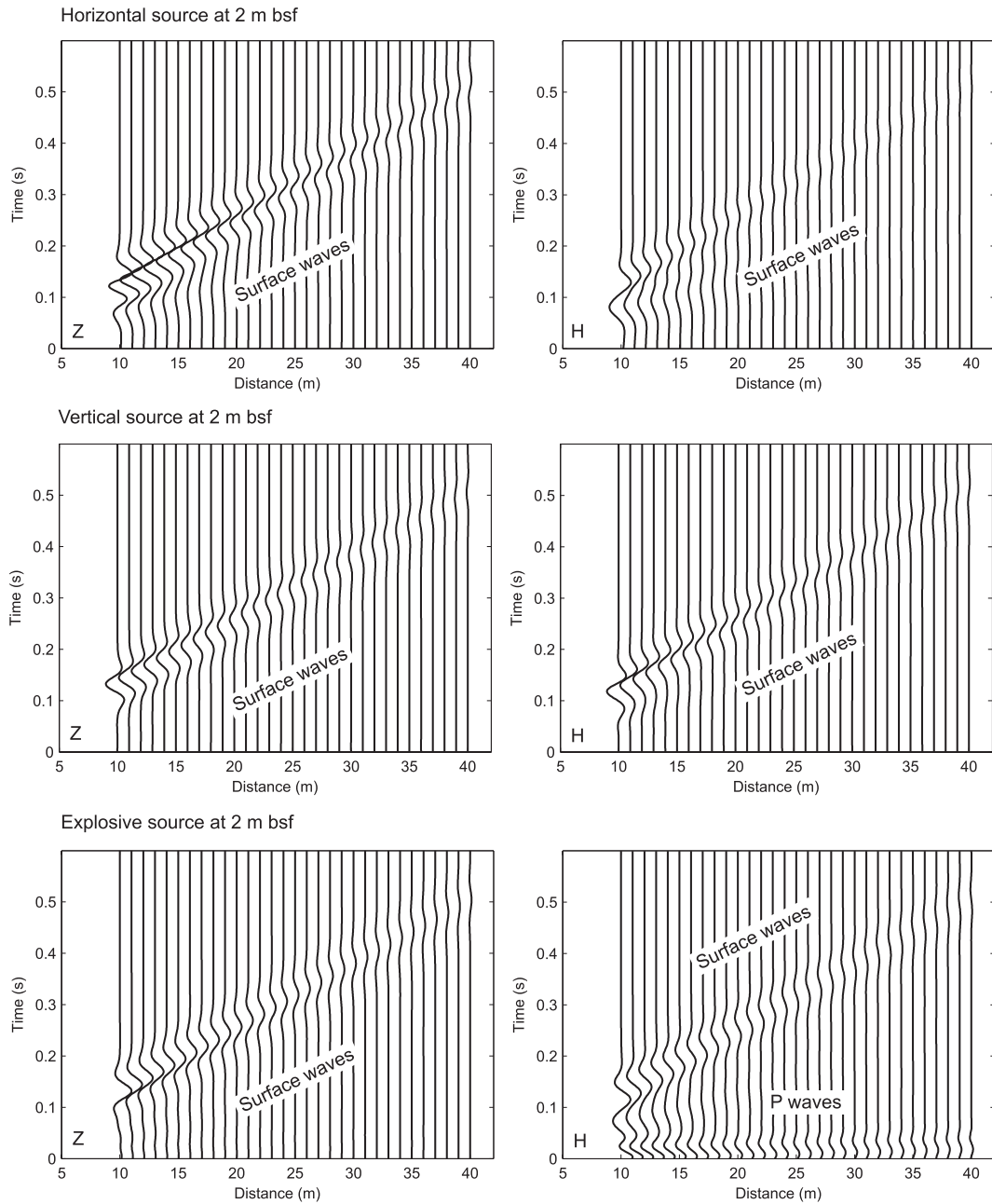


Figure 10. Numerical simulations using the SKB code (Dietrich 1988) for a horizontal, a vertical and an explosive source located at 2 m bsf (below seafloor), and sensors 1 cm within the sediments. The original numerical signals in displacement were differentiated once (velocity) and then normalized by the first numerical signal (distance: 10 m). H, horizontal motion; Z, vertical motion. Note the strong attenuation of *P* and surface waves.

Laboratory experiments, where gas (air) is injected in a granular media (sodosilica grains with diameters of 100 and 400 μm), have shown that gas escapes through numerous conduits that look like tree branches (Varas *et al.* 2009; Varas *et al.* 2011). Gas conduits seem to be intrinsically unstable, because, even without variations of the gas injection rate, conduits are created or closed continuously. The superficial sediments of the Sea of Marmara are mainly clay-rich cohesive sediments with particles smaller than 5 μm . Nevertheless, open conduits in compacting sediments are expected to be mechanically unstable except very close to the seafloor. We suspect that the opening and collapse of conduits or gas filled fractures could explain the characteristics of microevents (Fig. 3). Considering the low cohesion of superficial sediments, the vertical force

needed by the fluids to move up towards the seafloor is supposedly small. The main displacements are then produced by the sidewalls of the subvertical conduit. In addition, the conduits observed during laboratory experiments of gas injection in granular media (Varas *et al.* 2009; Varas *et al.* 2011) are generally nearly verticals. Explosion or vertical force types of source are still possible if a layer of higher cohesion is present on the pathway of the gas.

Then, our preferred mechanism consists of a subvertical fracture, pre-existent or not, gradually filled by gas within a porous and saturated medium (Fig. 12). The fracture is located close to the sediment-water interface. Gas pressure increases as the crack fills and progressively opens (step 0). When the fracture toughness threshold is reached, the gas will rise up in a moving crack,

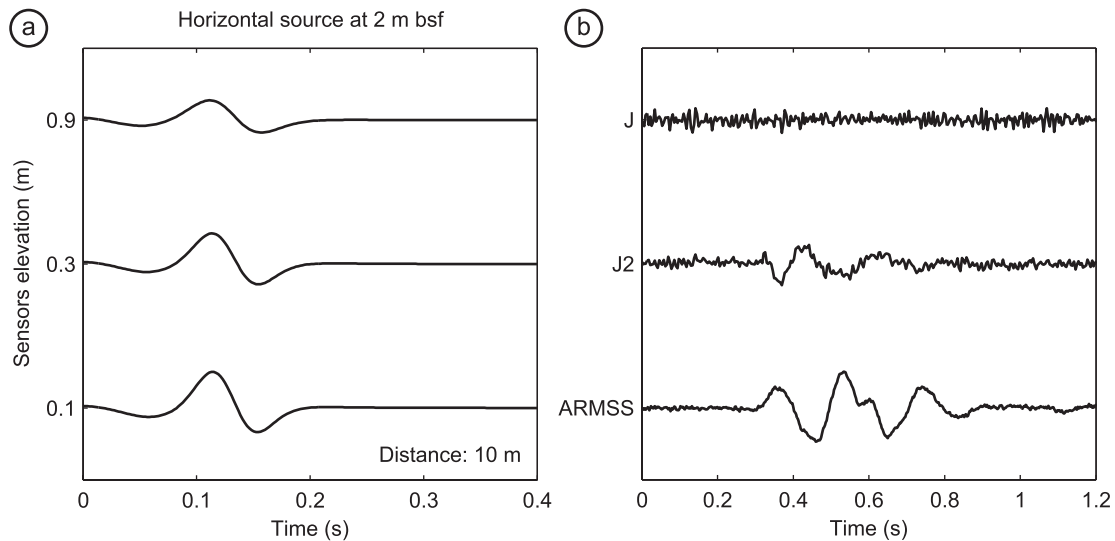


Figure 11. (a) Microevents numerical simulations for a horizontal source at 2 m bsf and sensors at 0.1, 0.3 and 0.9 m above the interface (distance: 10 m), showing the vertical attenuation of surface waves. (b) Hydrophone recordings of OBSs ARMSS (~ 0.05 m), J2 (~ 0.3 m) and J (~ 0.9 m), for three signals of similar corrected amplitudes ($\sim 15 \mu\text{m s}^{-1}$) recorded by these OBSs. The signals are normalized by those situated close to the sea water-sediments interface (0.1 m-ARMSS).

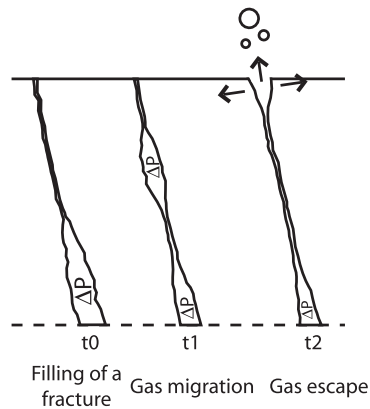


Figure 12. Schematic explanation in three steps of the mechanism proposed for the microevents source: gas migration and escape through a subvertical conduit.

reaching or not the sediment-water interface (step 1), where it can escape to the sea water (step 2) without major deformation of the sedimentary matrix (Johnson *et al.* 2002; Boudreau *et al.* 2005; Algar & Boudreau 2009). After the gas migration, the confining pressure will close the fracture. Fluid-filled crack models do not require venting, but focus mainly on the resonance characteristics of the cracks (e.g. Aki *et al.* 1977; Chouet 1986, 1988; Jousset *et al.* 2003). Hence, microevents can be generated as the gas migrates in the conduit, or by its expulsion at the seafloor. The partitioning of the signal recorded by the OBSs in horizontal and vertical motions will depend on fractures tilt and depth, and on wave propagation processes.

6.2 Interpretation of the microevents crisis

We identified two types of microevents: small impulsive, clustered events and larger amplitude oscillatory signals, which appear less frequently and display more variability and could correspond to Stoneley-Scholte waves.

Varas *et al.* (2009) described two regimes of bubbles emission in granular media depending on the gas injection rate. At low flow

rate, large and independent bubbles are formed ('bubbling regime'), whereas at high flow rate, small bubbles supplied by a continuous channel are produced ('open-channel regime'). Except the swarm recorded by OBS M, all OBSs displayed a low daily rate of microevents. We propose that the larger microevents correspond to the collapse of a cavity or fracture that trapped gas at a relatively shallow depth below the sediments. The crisis recorded by OBS M followed such an event and could, hypothetically, result from a nearby continuous flow of bubbles in an open-channel regime which followed the expulsion of the gas from the main cavity.

7 CONCLUSIONS

Numerous non-seismic microevents of short durations were recorded on different types of OBSs. These signals, of peak amplitudes comparable to those of earthquakes, were predominantly recorded by geophones. They were also recorded by those hydrophones situated less than a few tens of centimetres from the seafloor. Because the signals have similar characteristics (in terms of duration, frequency content), whatever the instrument and whatever the environment, it is very unlikely—if not impossible—that these microevents be related to instrumental artefacts, or 'fish bumps'.

The microevents are generally not correlated from one OBS to another, with one notable exception for the closest OBSs (~ 10 m apart). Moreover, microevents present a specific attenuation pattern, that is both horizontally in sediments and vertically in the water column.

Specific focus has been given to the microevents recorded by OBS M during the crisis that occurred on 2007 June 11–12. The presence of gas in the superficial layers and the source modelling we performed suggest that these microevents are likely related to gas-related processes from the seafloor, such as the opening and closure of a conduit induced by degassing near the subsurface. The present work shows that OBSs can detect episodes of gas accumulation and release in shallow sediment layers. In combination with piezometers and bubble recorders, OBS could be used in the Sea of Marmara to monitor the evolution of such episodes, hence to better understand

the relationships between deformation and non-seismic transients related to degassing from the seafloor layers near the fault zone.

Our work also confirms recent results obtained with multibeam acoustic systems operating in the water column mode, suggesting that free gas emissions from the seafloor are likely to be more widespread than previously thought.

ACKNOWLEDGMENTS

This work is part of the PhD thesis of JBT, co-funded by Total, Magnitude/BakerHughes and Ifremer. CGG Veritas kindly provided the data from the ARMSS, NEEDLE and SPAN. The work was conducted within the Marmara Demonstration Mission of the European Seafloor Observatory Network (ESONET) and benefited from financial support from both ESONET and Agence Nationale de la Recherche (project ANR/ISIS). Special acknowledgments to: the Captain and crew of Ifremer and ITU vessels (*R/V L'Atalante* and *R/V Yunuz*); Francis Cerda (Total), Thomas Bardainne (Magnitude, BakerHughes); Renaud Daures, Emmanuel Auger (CGGVeritas); Bach-Lien Hua, Pascal Pelleau, Ronan Apprioual and Yves Auffret (Ifremer); Jacques Talandier and Michel Dietrich.

REFERENCES

- Aki, K., Fehler, M. & Das, S., 1977. Source mechanism of volcanic tremor: fluid-driven crack models and their application to the 1963 Kilauea eruption, *J. Volc. Geotherm. Res.*, **2**, 259–287.
- Algar, C.K. & Boudreau, B.P., 2009. Transient growth of an isolated bubble in muddy, fine grained sediments, *Geochim. cosmochim. Acta*, **73**, 2581–2591, doi:10.1016/j.gca.2009.02.008.
- Alpar, B., 1999. Underwater signatures of the Kocaeli earthquake of 17 August 1999 in Turkey, *Turkish J. Mar. Sci.*, **5**, 111–130.
- Alpar, B. & Yüce, H., 1997. Short and tidal period sea-level variations along the Turkish Strait system, *Turkish J. Mar. Sci.*, **3**, 11–22.
- Armijo, R. et al., 2005. Submarine fault scarps in the Sea of Marmara pull-apart (North Anatolian Fault): implications for seismic hazard in Istanbul, *Geochem. Geophys. Geosyst.*, **6**, Q06009, doi:10.1029/2004GC000896.
- Biot, M.A., 1956. Theory of the propagation of elastic waves in a fluid saturated porous solid, 1, low-frequency range, *J. Acoustic Soc. Am.*, **28**, 168–178.
- Bone, Q. & Moore, R.H., 2008. *Biology of Fishes*, 3rd edn, Taylor & Francis, Abington, 478pp.
- Bouchon, M., 1981. A simple method to calculate Green's functions for elastic layered media, *Bull. seism. Soc. Am.*, **71**, 959–971.
- Boudreau, B.P. et al., 2005. Bubble growth and rise in soft sediments, *Geology*, **33**(6), 517–520, doi:10.1130/G21259.1.
- Bourry, C. et al., 2009. Free gas and gas hydrates from the Sea of Marmara, Turkey. Chemical and structural characterization, *Chem. Geol.*, **264**, 197–206, doi:10.1016/j.chemgeo.2009.03.007.
- Buskirk, R.E., Frohlich, C., Latham, G.V., Chen, A.T. & Lawton, J., 1981. Evidence that biological activity affects ocean bottom seismograph recordings, *Mar. Geophys. Res.*, **5**(2), 189–205.
- Campbell, K.W., 2009. Estimates of shear-wave Q and κ_0 for unconsolidated and semiconsolidated sediments in Eastern North America, *Bull. seism. Soc. Am.*, **99**, 2365–2392, doi:10.1785/0120080116.
- Chouet, B., 1986. Dynamics of a fluid-driven crack in three dimensions by the finite difference method, *J. geophys. Res.*, **91**(B14), 13 967–13 992.
- Chouet, B., 1988. Resonance of fluid-driven crack: radiation properties and implications for the source of long-period events and harmonic tremor, *J. geophys. Res.*, **93**, 4375–4400.
- Chouet, B., 1996. Long-period volcano seismicity: its source and use in eruption forecasting, *Nature*, **380**, 309–316, doi:10.1038/380309a0.
- Diaz, J., Gallart, J. & Gaspà, O., 2007. Atypical seismic signals at the Galicia Margin, North Atlantic Ocean, related to the resonance of subsurface fluid-filled cracks, *Tectonophysics*, **433**, 1–13, doi:10.1016/j.tecto.2007.01.004.
- Dietrich, M., 1988. Modeling of marine seismic profiles in the t-x and tau-p domains, *Geophysics*, **53**, 453–465, doi:10.1190/1.1442477.
- Dietrich, M. & Bouchon, M., 1985. Synthetic vertical seismic profiles in elastic media, *Geophysics*, **50**(2), 224–234.
- Dupré, S. et al., 2010. Widespread gas emissions in the Sea of Marmara in relation with the tectonic and sedimentary environments: results from ship-borne multibeam echosounder water column imagery (MARMESONET expedition, 2009), *Geophys. Res. Abstr.*, **12**, EGU2010–9429-2.
- Favretto-Anrès, N. & Rabau, G., 1997. Excitation of the Stoneley–Scholte wave at the boundary between an ideal fluid and a viscoelastic solid, *J. Sound Vib.*, **203**(2), 193–208.
- Ferrazzini, V., Chouet, B., Fehler, M. & Aki, K., 1990. Quantitative analysis of long-period events recorded during hydrofracture experiments at Fenton Hill, New Mexico, *J. geophys. Res.*, **95**(B13), 21 871–21 884.
- Géli, L., Bard, P.-Y. & Schmitt, D.P., 1987. Seismic wave propagation in a very permeable water-saturated surface layer, *J. geophys. Res.*, **92**, 7931–7944.
- Géli, L. et al., 2008. Gas emissions and active tectonics within the submerged section of the North Anatolian Fault zone in the Sea of Marmara, *Earth planet. Sci. Lett.*, **274**, 34–39, doi:10.1016/j.epsl.2008.06.047.
- Géli, L., Henry, P. & Çagatay, N., 2010. Marmesonet Leg1 Cruise Report, November 4th–November 25th, 2009. Available at: <http://www.esonet.marmara-dm.itu.edu.tr/> (accessed 2010 December).
- Haeckel, M., Boudreau, B.P. & Wallmann, K., 2007. Bubble-induced pore-water mixing: a 3-D model for deep porewater irrigation, *Geochim. cosmochim. Acta*, **71**, 5135–5154, doi:10.1016/j.gca.2007.08.011.
- Halbach, P., Holzbecher, E., Reichel, T. & Moche, R., 2004. Migration of the sulphate-methane reaction zone in marine sediments of the Sea of Marmara—can this mechanism be tectonically induced?, *Chem. Geol.*, **205**, 73–82, doi:10.1016/j.chemgeo.2003.12.013.
- Henry, P. & MarNaut Cruise Sci. Party, 2007. MarNaut Cruise of R/V L'Atalante Report. Available at: http://cdf.u-3mrs.fr/~henry/marmara/marnaut_public/marnaut_final_reports/ (last accessed 2012 June).
- Imren, C., Le Pichon, X., Rangin, C., Demirbağ, E., Ecevitöglu, B. & Görür, N., 2001. The North Anatolian Fault within the Sea of Marmara: a new interpretation based on multichannel seismic and multi-beam bathymetry data, *Earth planet. Sci. Lett.*, **186**, 143–158, doi:10.1016/S0012-821X(01)00241-2.
- Johnson, B.D., Boudreau, B.P., Gardiner, B.S. & Maass, R., 2002. Mechanical response of sediments to bubble growth, *Mar. Geol.*, **187**, 347–363.
- Jousset, P., Neuberg, J. & Sturton, S., 2003. Modelling the time-dependent frequency content of low-frequency volcanic earthquakes, *J. Volc. Geotherm. Res.*, **128**, 201–223, doi:10.1016/S0377-0273(03)00255-5.
- Jurkevics, A., 1988. Polarization analysis of three-component array data, *Bull. seism. Soc. Am.*, **78**, 1725–1743.
- Kanamori, H., Given, J.W. & Lay, T., 1984. Analysis of seismic body waves excited by the Mount St. Helens eruption of May 18, 1980, *J. geophys. Res.*, **89**(B3), 1856–1866.
- Kennet, B.L.N. & Kerry, N.J., 1979. Seismic waves in a stratified half-space, *Geophys. J. R. astr. Soc.*, **57**, 557–583.
- Le Pichon, X. et al., 2001. The main Marmara fault, *Earth planet. Sci. Lett.*, **192**, 595–616.
- Lokmer, I. & Bean, C.J., 2010. Properties of the near-field term and its effect on polarization analysis and source locations of long-period (LP) and very-long-period (VLP) seismic events at volcanoes, *J. Volc. Geotherm. Res.*, **192**, 35–47.
- Meunier, J. & Guennou, C., 1991. Computation of shear waves by integral methods in stratified media, in *Shear Waves in Marine Sediments*, pp. 495–502, eds Hovem, J.M., Richardson, M.D. & Stoll, R.D., Kluwer Academic Publishers, Dordrecht.
- Pontoise, B. & Hello, Y., 2002. Monochromatic infra-sound waves recorded offshore Ecuador: possible evidence of methane release, *TerraNova*, **14**, 425–435.
- Rangin, C., Demirbağ, E., Imren, C., Crusson, A., Normand, A., Le Drezen, E. & Le Bot, A., 2001. *Marine Atlas of the Sea of Marmara (Turkey)*, Ifremer, France.
- Rangin, C., Le Pichon, X., Demirbağ, E. & Imren, C., 2004. Strain localization in the Sea of Marmara: propagation of the North

- Anatolian Fault in a now inactive pull-apart, *Tectonics*, **23**(2), TC2014, doi:10.1029/2002TC001437.
- Sohn, R.A., Hildebrand, J.A., Webb, S.C. & Fox, C.G., 1995. Hydrothermal activity at the Megaplume Site on the Southern Juan de Fuca Ridge, *Bull. seism. Soc. Am.*, **85**(3), 775–786.
- Sultan, N., Voisset, M., Marsset, T., Vernant, A.M., Cauquil, E., Colliat, J.L. & Curinier, V. 2007. Detection of free gas and gas hydrate based on 3D seismic data and cone penetration testing: an example from the Nigerian Continental Slope, *Mar. Geol.*, **240**, 235–255, doi:10.1016/j.margeo.2007.02.012.
- Talandier, J. & Okal, E.A., 1996. T waves from underwater volcanoes in the Pacific Ocean: ringing witnesses to geyser processes?, *Bull. seism. Soc. Am.*, **86**(5), 1529–1544.
- Tary, J.B., 2011. Case studies on fluids and seismicity in submarine environments based on Ocean Bottom Seismometers (OBS) recordings from the Sea of Marmara and application to the Niger Delta, *PhD thesis*. Université de Bretagne Occidentale, available at: <http://archimer.ifremer.fr/doc/00034/14557/> (last accessed 2012 June).
- Tary, J.B., Géli, L., Henry, H., Natalin, B., Gasperini, B., Çomoglu, M., Çagatay, N. & Bardainne, T., 2011. Sea bottom observations from the western escarpment of the Sea of Marmara, *Bull. seism. Soc. Am.*, **101**, 775–791, doi:10.1785/0120100014.
- Toksöz, M.N. & Johnson, D.H., eds, 1981. Seismic wave attenuation, in *Geophysics Reprint Series, No. 2*, Society of Exploration Geophysicists, Tulsa, OK, 459pp.
- van Kessel, T. & van Kesteren, W.G.M., 2002. Gas production and transport in artificial sludge depots, *Waste Manage.*, **22**, 19–28.
- Varas, G., Vidal, V. & Géminard, J.C., 2009. Dynamics of crater formations in immersed granular materials, *Phys. Rev.*, **79**, 021301, doi:10.1103/PhysRevE.79.021301.
- Varas, G., Vidal, V. & Géminard, J.C., 2011. Venting dynamics of an immersed granular layer, *Phys. Rev.*, **83**, 011302, doi:10.1103/PhysRevE.83.011302.
- Vavryčuk, V., 1992. Polarization properties of near-field waves in homogeneous isotropic and anisotropic media: numerical modeling, *Geophys. J. Int.*, **110**, 180–190.
- Vidal, V., Géminard, J.-C., Divoux, T. & Melo, F., 2006. Acoustic signal associated with the bursting of a soap film which initially closes an overpressurized cavity, *Eur. Phys. J. B.*, **54**, 321–329, doi:10.1140/epjb/e2006-00450-0.
- Wang, Z., Street, R., Woolery, E. & Harris, J., 1994. Q_s estimation for unconsolidated sediments using first-arrival SH wave critical refractions, *J. geophys. Res.*, **99**, 13 543–13 551.
- Zakharia, M.E., 2002. Sub-bottom variability characterization using surface acoustic waves, in *Impact of Littoral Environmental Variability on Acoustic Predictions and Sonar Performance*, pp. 131–138, eds Pace, N.G. & Jensen, F.B. Kluwer Academic Publishers, Dordrecht.
- Zitter, T.A.C. *et al.*, 2008. Cold seeps along the main Marmara Fault in the Sea of Marmara (Turkey), *Deep-Sea Res.*, **55**, 552–570, doi:10.1016/j.dsr.2008.01.002.

SUPPORTING INFORMATION

Additional Supporting Information may be found in the online version of this article:

Table S1. Conversion factors for all OBSs hydrophone (counts to Pa) and vertical geophone (counts to $\mu\text{m s}^{-1}$).

Table S2. First eigenvector characteristics of the PCA performed on the complete data set. Per cent, data representativeness (energy); Freq., dominant frequency; Dur., duration. Waveforms and spectra corresponding to all the first eigenvectors are given in Fig. S6.

Figure S1. Response curve of the geophone Geospace GS-11D (natural frequency: 4.5 Hz). This geophone was used in OldOBS and MicrOBS instruments (J, J2, K, L and M; available at <http://www.geospacelp.com/index.php?id=142>). The damping value used during the MarNaut cruise in 2007 is 50 per cent (curve B).

Figure S2. Recordings of a seismic shot (2007 May 24, 07:04:21.6) by the 5 OBSs before and after intercalibration (see Fig. 1 for locations). Despite the resonance of OBS J2 geophones, the seismic shot amplitudes on OBSs J2 and J are in the same order of magnitude. Cor. Ampl., Corrected amplitudes.

Figure S3. Examples of microevents recorded by the OBS J, K, L, J2, ARMSS and SPAN. Amplitudes were corrected according to the methodology described in Section 2. For each instrument, the recordings of the hydrophone (H) and the three geophones are shown (horizontal: X, Y; vertical: Z). ARMSS and SPAN recordings show a microevent simultaneously recorded by the two instruments (same origin time). Note the resonance of the geophones of OBSs J2 and SPAN.

Figure S4. Probability density function showing the number of microevents (N_{ME}) per interval of 20 min in function of the hour of the day, (a) for each instrument deployed during the MarNaut cruise in 2007 and (b) combined in a single probability density function for all OBSs. In (b), a slight increase of the average N_{ME} from noon to midnight and a peak at 13 h are visible, but no clear daily periodicity.

Figure S5. (Top) Selection of 30 microevents recorded by OBS M during the crisis in the frame of reference of the polarization ellipsoid (components x_1 , x_2 and x_3). (Bottom) Frequency spectrum of one of the microevents presented above (also shown in Fig. 3b).

Figure S6. Waveforms (left) and normalized spectrum (right) corresponding to the first eigenvector of the PCA applied to the microevents recorded by each OBS (components x_1 , x_2 and x_3). The microevents temporal series were rotated before the PCA. Representativeness, duration and dominant frequency of all first eigenvectors are given in Table S2.

Figure S7. P -wave velocity and density of the sediments for the upper 10 m of sediments (mbsf, meters below seafloor), measured by the MSCL core logging system on a core located close to OBS J.

Please note: Wiley-Blackwell are not responsible for the content or functionality of any supporting materials supplied by the authors. Any queries (other than missing material) should be directed to the corresponding author for the article.